Petroleum Science 23 (2026) 5648–5661

Contents lists available at ScienceDirect

Petroleum Science

journal homepage: www.keaipublishing.com/en/journals/petroleum-science

Original Paper

A novel ultra-high-temperature emulsifier stable at 250 °C for oil-based drilling fluids: Synthesis, performance, and mechanism

Quan-De Wang [a,b], Guan-Cheng Jiang [a,b,*], Teng-Fei Dong [b,c], Sheng-Ming Huang [a,b], Yin-Bo He [a,b], Li-Li Yang [a,b], Qi Feng [a,b], Hua-Yan Mu [a,b]

[a] College of Petroleum Engineering, Key Laboratory of Petroleum Engineering, China University of Petroleum (Beijing), Beijing, 102249, China
[b] State Key Laboratory of Petroleum Resources and Engineering, China University of Petroleum (Beijing), Beijing, 102249, China
[c] College of Science, China University of Petroleum (Beijing), Beijing, 102249, China

ARTICLE INFO

Article history:
Received 2 December 2025
Received in revised form
20 January 2026
Accepted 7 April 2026
Available online 13 April 2026

Edited by Xi Zhang

Keywords:
Exploration
Emulsifier
Temperature resistance
Mechanism

ABSTRACT

The ultra-high temperature conditions encountered in deep oil and gas exploration represent a critical challenge to oil-based drilling fluid (OBDF) technology. Conventional emulsifiers suffer from rapid deterioration of interfacial stability under harsh environments exceeding 200 °C, significantly increasing the risk of emulsion breakdown and creating a critical bottleneck for ultra-high temperature drilling operations. To address this challenge, this study aimed to develop a novel high-efficiency ultra-high temperature emulsifier (UHT-EM). The UHT-EM was successfully synthesized via a three-step method, and its molecular structure and excellent thermal stability were confirmed by Fourier-Transform Infrared Spectroscopy (FT-IR) and Thermogravimetric Analysis (TGA). The key synthesis process was optimized using response surface methodology, establishing optimal conditions (molar ratio 1.8, temperature 53 °C, catalyst dosage 13.4%) with an actual yield of 85.23%. Performance evaluation demonstrated that UHT-EM significantly reduced oil-water interfacial tension. At a dosage of 1.0%, the emulsion maintained optimal rheological properties and electrical stability (ES > 1400 V) after thermal aging at 230 °C. Systematic temperature resistance tests revealed that the UHT-EM system maintained structural stability at 250 °C, while experiencing sharp performance deterioration at 260 °C due to interfacial film disruption. Microscopic analysis revealed that stabilization mechanism arose from a dense interfacial adsorption layer, while interface failure was caused by intensified molecular thermal motion under high-temperature conditions. The innovation of this research lay in developing a novel emulsifier with well-defined temperature resistance and revealing its stabilization and failure mechanisms through multi-scale analysis, providing crucial material support and theoretical foundation for ultra-high temperature drilling fluid design.

1. Introduction

As global oil and gas exploration and development continue to advance into deeper formations, the number of deep and ultra-deep wells keeps growing, with the upper limit of downhole temperatures being repeatedly surpassed (Sun et al., 2024; Meng et al., 2025). In such extreme high-temperature environments, the stability of drilling fluid systems directly impacts the safety, efficiency, and cost of drilling operations (Zhang et al., 2025; Aftab and Syahrir, 2025). OBDFs have become the preferred choice for drilling complex deep formations due to their exceptional shale suppression, wellbore stability, reservoir protection capabilities, excellent lubricity, and high drilling efficiency (Abdullahi et al., 2025; Bai et al., 2025). However, high-temperature and even ultra-high-temperature (typically exceeding 200 °C) downhole conditions severely challenge their performance stability (Wang et al., 2022; Chen et al., 2022). One of the most critical bottlenecks lies in the thermal failure of emulsifiers. Emulsifiers form the foundation for constructing and stabilizing water-in-oil (W/O) drilling fluids. They create an adsorbed layer at the oil-water interface that prevents droplet coalescence, thereby ensuring the

* Corresponding author.
E-mail address: m15600263100_1@163.com (G.-C. Jiang).
Peer review under the responsibility of China University of Petroleum (Beijing).

https://doi.org/10.1016/j.petsci.2026.04.009

kinetic stability of the emulsion system (Zhang et al., 2017; Ni et al., 2023).

The mechanism of emulsifiers primarily involves the oriented adsorption of amphiphilic molecules at the oil-water interface and the formation of an interfacial film (Liu et al., 2020; Zhu et al., 2025). Hydrophilic groups (such as sulfonic acid groups or amides) insert into the aqueous phase, while hydrophobic groups (such as long-chain alkanes) extend into the oil phase, thereby forming a tightly packed adsorbed layer (Jiang et al., 2016). The oil-water interfacial film not only significantly reduces interfacial tension and promotes the dispersion of emulsion droplets but also effectively hinders droplet collisions and coalescence through steric hindrance and electrostatic repulsion, enhancing the emulsion's kinetic stability (Lei et al., 2025; Liu et al., 2026). However, under high-temperature conditions, the thermal motion of emulsifier molecules intensifies, posing severe challenges to the compactness and strength of the interfacial film (Liu et al., 2022). Molecules may undergo desorption or even degradation, leading to film rupture and emulsion destabilization (Sun and Wang, 2025). Therefore, the core of developing ultra-high-temperature emulsifiers lies in designing molecular structures with higher interfacial adsorption energy and thermal stability, while thoroughly elucidating interfacial behavior and failure mechanisms under extreme temperatures (Li et al., 2023; Zhao et al., 2023). Although existing research has made some progress, significant gaps remain in the study of ultra-high-temperature emulsifiers. Most conventional emulsifiers exhibit a sharp decline in interfacial stability beyond 230 °C (Ma et al., 2025). For instance, sulfonate-based emulsifiers may undergo molecular chain breakage above 200 °C, leading to reduced electrical stability and failure in filtration control (Sun et al., 2018). Furthermore, current understanding of high-temperature failure mechanisms remains incomplete. Key processes such as molecular conformation changes, interfacial film strength decay kinetics, and adsorption-desorption equilibrium lack systematic and quantitative investigation, with most studies confined to macroscopic performance levels (Mona et al., 2023; Wang et al., 2022). In terms of synthesis, the preparation of high-performance emulsifiers often involves multi-step reactions and harsh conditions, facing challenges such as low yields, difficult cost control, and poor batch consistency. Therefore, an efficient and continuously producible process system remains to be established (Xie et al., 2026; Huang et al., 2026).

To address the failure of emulsifiers under ultra-high-temperature conditions, researchers worldwide have developed various types of high-temperature-resistant emulsifiers. For instance, Tu (2016) developed a sulfonate emulsifier through chlorination, alkylation, and sulfonation reactions, exhibiting a high-temperature, high-pressure filtrate loss of only 4.2 mL after aging at 180 °C. Du (2020) developed a sulfonate emulsifier, NGE-1, which maintained stable performance after 72 h of aging at 200 °C. Additionally, Halliburton's EZ-MUL emulsifier withstands temperatures up to 260 °C while delivering stable emulsification performance at lower dosage rates (Marinescu et al., 2014). Despite the progress summarized above, significant research gaps persist in the development of emulsifiers for ultra-high-temperature drilling fluids. First, the operational temperature limit of most conventional emulsifiers rarely exceeds 230 °C, leaving a critical need for molecules with demonstrable stability above 230 °C. Second, the understanding of high-temperature failure mechanisms—such as molecular conformational changes, interfacial film strength decay kinetics, and adsorption–desorption equilibria—remains largely qualitative and fragmented. Third, synthesis processes for high-performance emulsifiers often lack systematic optimization, facing challenges in yield, reproducibility, and scalability.

To address these gaps, this study was designed and synthesized a novel ultra-high-temperature emulsifier, UHT-EM. The key innovations of this work were threefold: (1) The molecular architecture, incorporating a diphenylethane-bridged aromatic core, long alkyl chains, and sulfonate groups, was tailored to sustain interfacial integrity up to 250 °C. (2) Response surface methodology was employed to quantitatively optimize the synthesis, establishing a reproducible route. (3) A multi-scale evaluation—correlating macroscopic rheology and electrical stability with microscopic wettability, droplet-size evolution, and interfacial behavior—provided a mechanistic understanding of both stabilization and failure under extreme thermal conditions. This study not only delivers a high-performance emulsifier material but also offers a comprehensive framework for the design, optimization, and evaluation of next-generation thermal-resistant additives for deep and ultra-deep drilling.

2. Experimental

2.1. Materials

Lauric acid (analytical grade), thionyl chloride (analytical grade), diphenylethane (analytical grade), carbon disulfide (analytical grade), chlorosulfonic acid (analytical grade), aluminum chloride (analytical grade), calcium hydroxide (analytical grade), and petroleum ether (analytical grade) were all purchased from Beijing Xinbaohai Chemical Technology Co., Ltd. Sodium hydroxide, Span80 and ethanol were purchased from Shanghai McLean Biochemical Technology Co., Ltd. Calcium oxide was purchased from Beijing Inokai Technology Co., Ltd. The auxiliary emulsifier was prepared in-house in the laboratory. No. 0 diesel fuel and high-temperature emulsifier (BCEM) were sourced from Beijing Shida Bocheng Co., Ltd.

2.2. Synthesis of UHT-EM

The synthesis of UHT-EM mainly involves three steps, namely acylation reaction, Friedel–Crafts alkylation reaction, and sulfonation neutralization reaction. The reaction process is shown in Fig. 1.

2.2.1. Acylation reaction

100 g of lauric acid was weighed and added into a three-necked flask with a condensation reflux device, and the lauric acid was melted after the temperature was raised to 60 °C. With stirring on, 74.63 g of sulfoxide chloride was slowly added to the lauric acid through a constant-pressure dropping funnel (finished within 1 h), and then the reaction was heated up to 85–90 °C and refluxed for 3 h. At the end of the reaction, the reaction was cooled down to room temperature. The excess $SOCl_2$ was removed by distillation under reduced pressure, and the light-yellow product lauryl chloride was obtained, denoted as 12-1.

2.2.2. Friedel–Crafts alkylation reaction

23.5 g of diphenylethane and 20 g of anhydrous aluminum trichloride were weighed and quickly added into a three-necked flask with a certain amount of CS_2, and fully stirred to dissolve. The temperature of the ice-water bath was controlled at 5–10 °C, 45 g of lauryl chloride was added slowly by dropping in a constant pressure dropping funnel (within 30 min), and the reaction was heated to reflux at 45 °C for 3 h. At the end of the reaction, the reaction was cooled to room temperature. The crude product was quenched with a mixture of 100 g of crushed ice and dilute hydrochloric acid, followed by repeated rinsing with dilute hydrochloric acid for 2–3 times, and then washed with dilute sodium

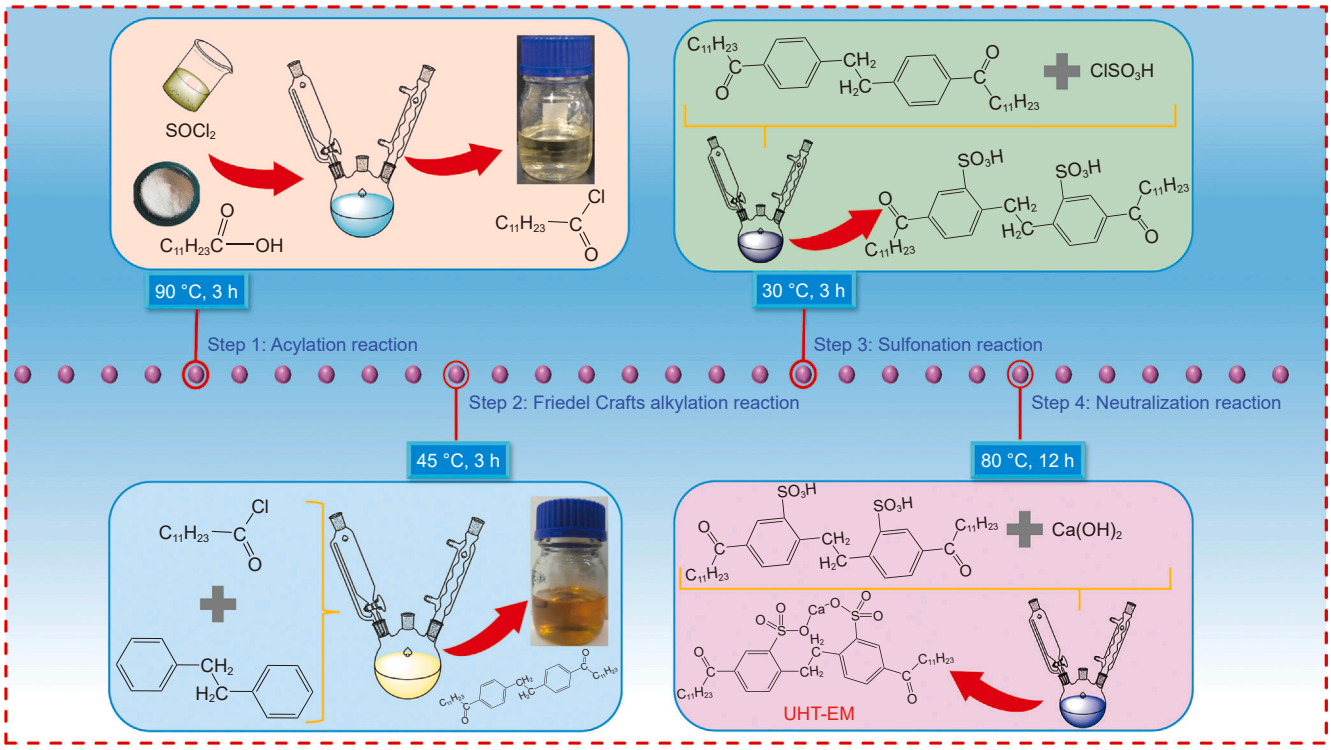

Fig. 1. Schematic diagram of UHT-EM synthesis.

hydroxide and distilled water for several times until it was neutral. The crude product was dissolved with petroleum ether, and the CS_2 and petroleum ether were removed by distillation under reduced pressure to obtain the product 1,1'-(ethane-1,2-diylbis(4,1-phenylene))bis(dodecan-1-one), denoted as 12-2.

2.2.3. Sulfonation neutralization reaction

35 g of 1,1'-(ethane-1,2-diylbis(4,1-phenylene))bis(dodecan-1-one) was weighed and added to a three-necked flask and dissolved with petroleum ether. The temperature of ice water bath was controlled at 5–10 °C, and 18.67 g of chlorosulfonic acid was slowly added by dripping through a constant pressure dropping funnel (finished within 30 min), and the reaction was warmed up to 30 °C for 4 h. At the end of the reaction, a certain amount of distilled water was added to separate the acid, and the organic acid was obtained. A certain amount of solvent (ethanol/water) was added to the organic acid and stir until uniform. Calcium hydroxide was added to control the pH between 7 and 9. The mixture was heated to 80 °C and reacted for 12 h. After cooling to room temperature, the solvent was removed by vacuum distillation. The product was dried and pulverized to yield 6,6'-(ethane-1,2-diyl)bis(3-dodecanoylbenzenesulfonate), denoted as 12-3.

2.3. Optimized design

The synthesis of UHT-EM mainly involved three reactions. The Friedel–Crafts alkylation reaction (intermediate reaction) had an extremely important impact on the yield of the target product. In addition, the Friedel–Crafts alkylation reaction was more complex compared to the other two-step reactions. Therefore, it is necessary to optimize the synthesis process of UHT-EM.

Firstly, the main influences on the response were determined by a one-way experiment. Then, optimization experiments were designed by response surface methodology. Finally, the optimal conditions for the reaction were determined. The three influencing factors identified in this study were molar ratio, temperature and catalyst addition. In addition, the tertiary variables were coded as −1, 0, and 1, as shown in Table 1.

The optimized experimental protocols and yields of the synthesis process of UHT-EM are shown in Table 2. A second order polynomial response equation was designed and developed by Box-Behnken in order to analyze the relationship between the variables. Typically, the response surface equation is shown in Eq. (1) below (Li et al., 2018). Where Y is the value of the dependent variable, β_0 is the regression constant, the independent variables are represented by X_i and X_j, and β_i, β_i and β_{ij} represent the first-order linear regression coefficients, the quadratic regression coefficients, and the interaction effect coefficients, respectively.

$$Y = \beta_0 + \sum_{i=1}^{K} \beta_i X_i + \sum_{i=1}^{K} \beta_{ii} {X_i}^2 + \sum_{i=1}^{K} \sum_{i \neq j}^{K} \beta_{ij} X_i X_j \quad (1)$$

2.4. Molecular characterization of UHT-EM

The molecular structure characteristics of UHT-EM were analyzed using FT-IR. Samples were scanned using a MAGNA-560 spectrometer within the wavenumber range of 400–4000 cm^{-1} to obtain their infrared absorption spectra (Wang et al., 2025). The thermal stability of UHT-EM was determined via TGA using a

Table 1
Actual values and coding of independent variables.

Factor	Code	Level		
		−1	0	1
Molar ratio	X_1	2:1.5	2:1.25	2:1
Temperature, °C	X_2	45	55	65
Catalytic dosage, %	X_3	5	10	15

Table 2
Box-Behnken experimental design and yields.

Number	Molar ratio	Temperature, °C	Catalytic dosage, %	Yield, %
1	0	−1	1	77.62
2	0	1	−1	80.52
3	0	0	0	85.79
4	1	0	−1	80.56
5	0	0	0	85.52
6	0	−1	−1	75.60
7	0	1	1	84.74
8	0	0	0	85.27
9	1	0	1	83.38
10	−1	0	1	78.18
11	−1	0	−1	76.42
12	−1	1	0	78.75
13	0	0	0	84.88
14	0	0	0	85.41
15	1	−1	0	76.11
16	1	1	0	83.48
17	−1	−1	0	74.80

NETZSCH-STA 449F5 TGA instrument. The procedure was as follows: 5–10 mg of sample was weighed and placed in the instrument's standard alumina crucible. The test was conducted in a dynamic nitrogen atmosphere. The temperature program was set to start at 30 °C and linearly increase at a rate of 10 °C/min to a final temperature of 600 °C. Throughout the experiment, the system continuously monitored and recorded the sample's TG curve (Lei et al., 2024).

2.5. Oil water interface tension test

Firstly, a mixture of 0# diesel fuel with different concentrations of emulsifiers was prepared as an oil phase solution and 30% $CaCl_2$ solution as an aqueous phase sample. Then, the interfacial tension between the oil and aqueous phases was measured by the hanging drop method on an OCA25 tensiometer. The test temperature was 60 °C and the rotational speed was 5000 rpm/min (Wang et al., 2022).

2.6. Preparation of oil-based drilling fluid

The base OBDF was prepared according to the following procedure. First, a specified amount of UHT-EM, 2% secondary emulsifier, and 5% calcium oxide (CaO) were added to 240 mL of No. 0 diesel oil. The mixture was stirred at 12,000 rpm for 40 min to form a homogeneous dispersion. Then, 60 mL of 30% calcium chloride ($CaCl_2$) solution was introduced into the mixture, followed by further stirring at 12,000 rpm for 20 min to complete the emulsification process (Yang et al., 2025). The resulting fluid was stored for subsequent use.

2.7. The temperature resistance of UHT-EM

To systematically evaluate the temperature resistance of the UHT-EM, this study employed a methodology combining high-temperature aging tests with analysis of rheological properties and ES. First, emulsions containing varying amounts of UHT-EM were aged at 230 °C for 16 h. Their rheological properties and ES were then measured to investigate the impact of emulsifier dosage on the high-temperature stability of the emulsions. Based on these findings, the emulsifier dosage that demonstrated optimal performance was selected for further investigation. The emulsion containing this dosage was subsequently aged at different temperatures ranging from 230 °C to 260 °C for 16 h. The changes in its rheological properties and ES were then measured to evaluate the tolerance limit and structural stability of the emulsifier system under ultra-high-temperature conditions. By analyzing the evolution of rheological parameters with varying temperature and dosage, combined with the trends in ES, a comprehensive assessment was made regarding the emulsifier's applicable operating window and its failure mechanisms at elevated temperatures. This study provides essential experimental evidence for the design of ultra-high-temperature drilling fluid systems.

2.8. Wetting performance

The strength characteristics of interfacial facial mask of water in oil (W/O) emulsion stabilized by ultra-high temperature emulsifier were characterized by contact angle measurement. The emulsions were first prepared using the emulsifier and subjected to a series of high-temperature aging treatments. Subsequently, the contact angle of aged samples on glass slides was precisely measured using a JC2000D5M contact angle tester. The fundamental principle of this measurement is that an intact and robust interfacial film effectively prevents droplet spreading, resulting in a larger contact angle. Therefore, the contact angle value serves as a direct indicator of the structural strength and stability of the interfacial film, enabling investigation into its high-temperature stabilization mechanism (Feng et al., 2025).

2.9. Particle size distribution of emulsions

To investigate the interfacial stabilization mechanism of UHT-EM at the microscopic level, this study further analyzed the particle size distribution of emulsions treated at different aging temperatures. Specifically, emulsion samples containing the optimal amount of UHT-EM were subjected to 16 h of high-temperature aging within the range of 230 °C to 260 °C. Subsequently, a laser diffraction particle size analyzer was employed to determine their particle size distribution, yielding key characteristic data such as particle size distribution curves and cumulative distribution curves. By systematically analyzing the peak shape, peak position, distribution width, and cumulative curve slope of distribution curves at different temperatures, the uniformity of emulsion droplet size and changes in aggregation state are evaluated. This correlates and elucidates the stability and potential failure behavior of emulsifier interfacial films under ultra-high temperature conditions, providing microscopic evidence for understanding macroscopic performance changes (Nilanjan et al., 2018).

2.10. Performance evaluation of drilling fluid

The rheological properties of the OBDF were measured using a ZNN-D6B six-speed rotational viscometer in accordance with American Petroleum Institute (API) standards (Wang et al., 2022). The dial readings were recorded at rotational speeds of 600 rpm and 300 rpm, denoted as $\phi 600$ and $\phi 300$, respectively. The apparent viscosity (AV, mPa·s), plastic viscosity (PV, mPa·s), and yield point (YP, Pa) were then calculated based on the following Eq. (2)–(4).

$$AV = \phi 600/2 \tag{2}$$

$$PV = \phi 600 - \phi 300 \tag{3}$$

$$YP = (\phi 300 - PV)/2 \quad (4)$$

2.11. Electrical stability

According to the national standard GB/T16783.2-2012 “On site testing of drilling fluids for petroleum and natural gas industries - Part 2: Oil based drilling fluids”. The ES of the emulsion was tested three times and the data was recorded.

3. Result and discussion

3.1. FT-IR

The molecular functional groups of UHT-EM and its synthetic intermediates were characterized by FT-IR spectroscopy (Fig. 2). In intermediate 12-1, the strong peak at 1796 cm^{-1} corresponded to the C=O stretching vibration of the acyl chloride group. Peaks at 2923 cm^{-1} and 2854 cm^{-1} were attributed to asymmetric C–H stretching vibrations of $–CH_3$ and $–CH_2$. Additionally, a weak but distinct peak near 720 cm^{-1} was assigned to the in-plane rocking vibration of the $–(CH_2)_n–$ ($n \geq 4$) segments of the straight-chain alkane, indicating the presence of a long alkyl chain (see Fig. 3).

In intermediate 12-2, the acyl chloride peak at 1796 cm^{-1} disappeared, while two new carbonyl stretches emerged at 1730 cm^{-1} and 1682 cm^{-1}, indicating conversion to a ketone functionality. Aromatic C–H stretching was observed at 3034 cm^{-1}, and ring skeletal vibrations appear near 1605 cm^{-1} and 1580 cm^{-1}, confirming the benzene ring structure. The persistence of alkyl C–H stretches (2923 cm^{-1}, 2850 cm^{-1}) and the CH_2 bending mode at 1465 cm^{-1} further verified the retention of the dodecyl chain.

For intermediate 12-3, the most notable change was the appearance of strong, broad bands at 1186 cm^{-1} and 1131 cm^{-1}, assigned to asymmetric stretching vibrations of the $–SO_3H$ group. Additional confirmatory peaks included S–O stretching at 1048 cm^{-1} and aromatic C–H out-of-plane bending at 829 cm^{-1}, which together confirmed successful sulfonation of the benzene ring. Aromatic ring vibrations (~1603 cm^{-1}) and alkyl C–H modes remained present, whereas the ketone C=O stretches were likely slightly shifted or partially obscured by the intense sulfonate absorptions (Wang et al., 2023). The results indicated that the molecular structure of the target UHT-EM was essentially consistent with the intended design.

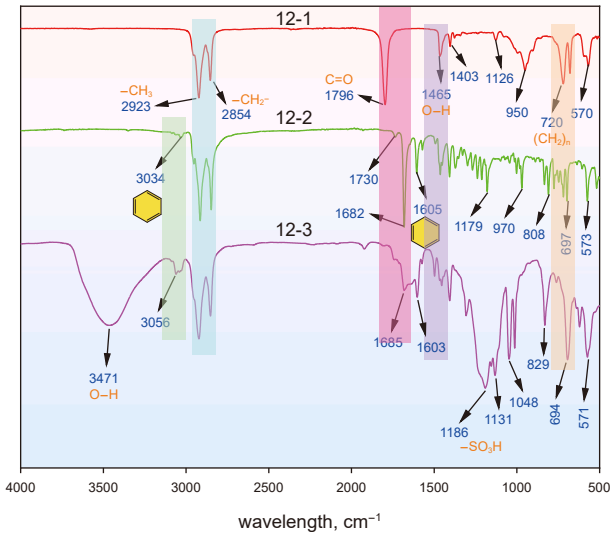

Fig. 2. FT-IR analysis of UHT-EM.

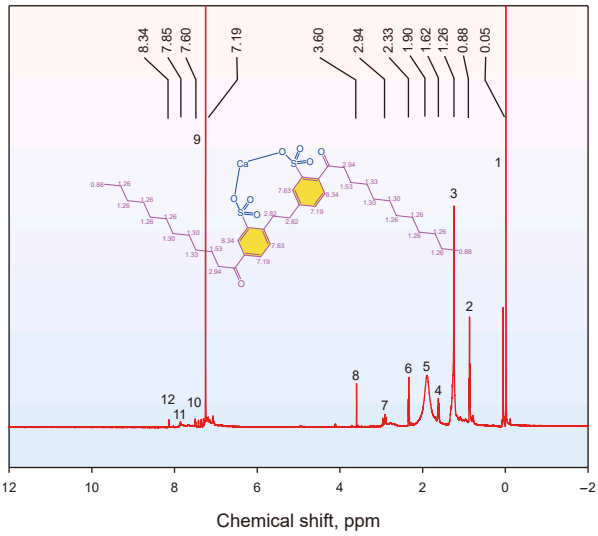

Fig. 3. ^{1}H-NMR spectrum of UHT-EM.

3.2. ^{1}H NMR

The NMR hydrogen spectrum of the product clearly assigned the chemical shifts of characteristic functional groups, showing excellent agreement with the molecular structure of UHT-EM, as shown in Fig. 3. In the aromatic region (δ 6.0–8.5 ppm), distinct aromatic proton signals (δ 8.34, 7.85, 7.60, 7.19) were observed, with significant downfield shifts indicated the presence of strong electron-withdrawing substituents ($–SO_3H$ and –C=O) attached to the benzene ring. In the region corresponding to carbonyl and methylene groups (δ 1.9–4.0 ppm), resonances at δ 3.60 and 2.94 were assigned to the methylene group linked to the carbonyl ($–CH_2–C=O$) and the methylene group adjacent to the aromatic ring ($–CH_2$-Ar), respectively. In the long-chain alkyl region (δ 0.5–1.8 ppm), a strong peak at δ 1.26 corresponded to the repetitive methylene protons ($–CH_2–$) within the alkyl chain, while a triplet at δ 0.88 was attributed to the terminal methyl group ($–CH_3$) (Bhola and Vikas, 2020). These spectral features collectively confirmed that the UHT-EM contained a long-chain alkyl group, a ketone moiety, and a benzenesulfonate group, which was fully consistent with the expected structure of the target compound.

3.3. TGA

The thermogravimetric curve of the synthesized UHT-EM is shown in Fig. 4. It can be seen from Fig. 4 that the thermogravimetric curve of UHT-EM had three main weight loss stages from room temperature (RT) to 600 °C. First, the first weight loss stage was from RT to T_1 with a mass loss of 2.4%. This part of the mass loss is mainly the volatilization of adsorbed water on the surface of UHT-EM. Secondly, the second stage of weight loss was from T_1 to T_2 with a mass loss of 4.2% and a maximum weight loss of 0.89%/min at 355.7 °C. The quality loss at this stage corresponds to the breakage and pyrolysis of the long dodecanoyl chains in the molecular structure. Then, the third stage was from T_2 to T_3 with a mass loss of 13.4% and a maximum weight loss rate of 2.85%/min at 451.3 °C. This is attributed to the complete decomposition and carbonization of core structures such as aromatic ring frameworks, calcium sulfonate functional groups, and ethylene linking bridges in the molecule. It is worth noting that even at a final temperature

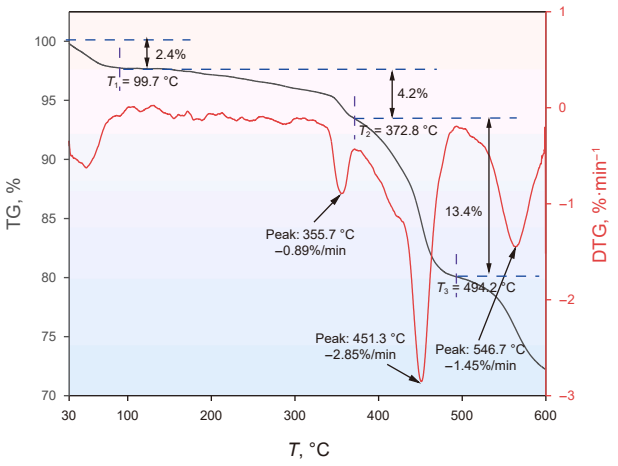

Fig. 4. TG analysis of UHT-EM.

of 600 °C, the sample still maintains a high residual rate of about 70%, further confirming the extremely high thermal stability of its molecular structure (Liu et al., 2022). This indicated that the UHT-EM was fully suitable for the application requirements of ultra-high temperature oilfield environments.

3.4. Univariate analysis

The yield of the key reaction was mainly affected by temperature, molar ratio and catalyst addition. It was therefore necessary to determine the range of optimum values for each factor through one-way experiments, the results of which are shown in Fig. 5.

Fig. 5(a) shows the effect of temperature on yield under certain molar ratios and catalyst dosages. It can be seen from Fig. 5(a) that as the temperature increased, the yield first increased and then tended to stabilize. The results showed that the yield reached its maximum at a reaction temperature of 53 °C. This is mainly attributed to effective collisions between molecules, which intensified the breaking of old bonds and the generation of new bonds, resulting in higher yields.

Fig. 5(b) shows the effect of molar ratio on the yield at a certain temperature and catalyst addition. It can be seen from Fig. 5(b) that as the molar ratio increased, the yield increased and then tended to stabilize. The results showed that the maximum yield was reached at a molar ratio of 1.7. This is mainly attributed to the excess of diphenylethane promoting the forward reaction, accelerating the reaction rate, and increasing the reaction yield. Meanwhile, after the consumption of dodecanoyl chloride, the yield tended to stabilize with little change.

Fig. 5(c) shows the effect of catalyst dosage on yield at a certain temperature and molar ratio. It can be seen from Fig. 5(c) that with the increase of catalyst dosage, the yield first increased and then decreased. The results indicated that a higher yield could be achieved when the catalyst dosage was 12%. This is mainly attributed to the fact that under appropriate catalyst dosage, the activation energy of the reaction would be reduced, the reaction rate would be accelerated, and the yield would be increased. At the same time, when the amount of catalyst added reached a certain value, the effect of catalyst on the reaction rate was limited, and there may be catalyst inclusions and products that were removed during the cleaning process.

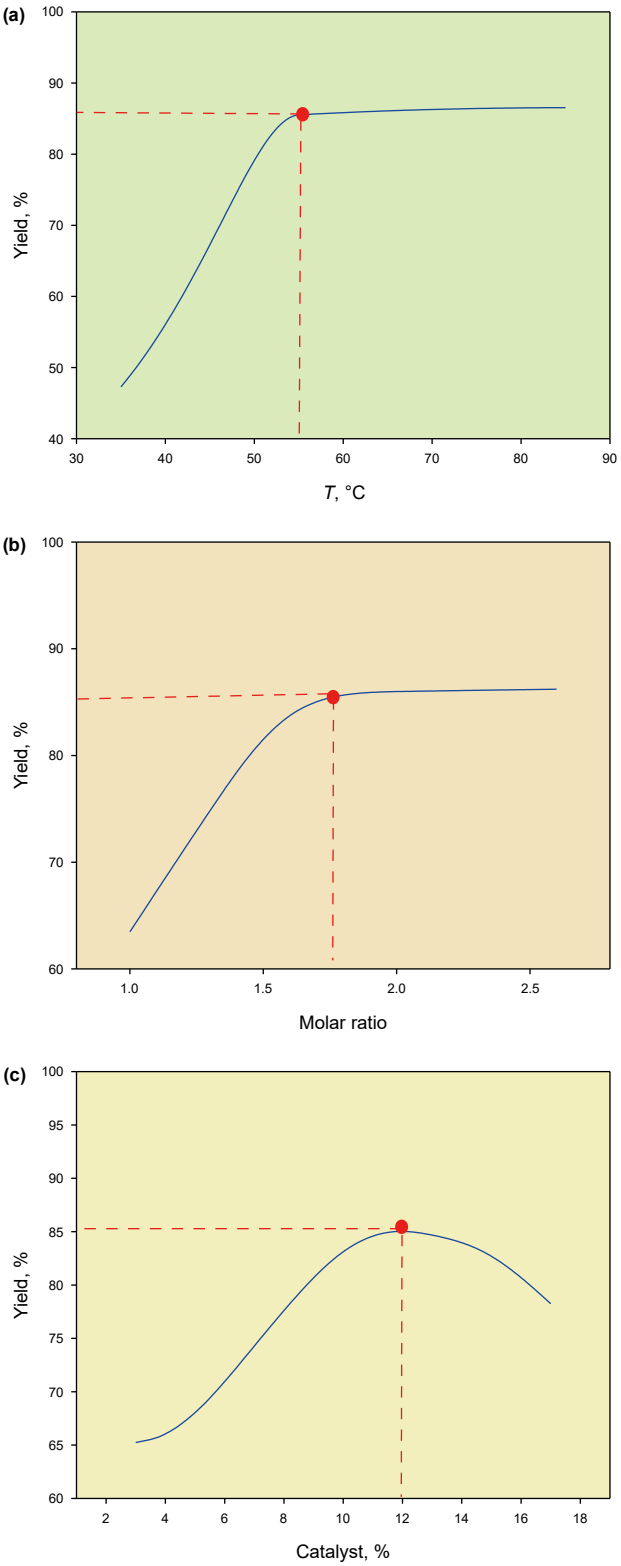

Fig. 5. The effect of reaction conditions on yield ((**a**) is the effect of reaction temperature on yield, (**b**) is the effect of molar ratio on yield, (**c**) is the effect of catalyst dosage on yield).

3.5. Variance analysis and regression model

The relationship between process parameters and yield was analyzed by Box-Behnken module and a multivariate fitted regression equation was developed. The second-order response surface equation is shown in Eq. (5). In the formula, Y is the yield, X_1 is the molar ratio, X_2 is the temperature and X_3 is the amount of catalyst added.

$$Y = 85.37 + 1.92X_1 + 2.92X_2 + 1.35X_3 + 0.855X_1X_2 + 0.265X_1X_3 + 0.55X_2X_3 - 3.54{X_1}^2 - 3.55{X_2}^2 - 2.2{X_3}^2 \quad (5)$$

Generally, the accuracy of models established using response surface methodology can be determined by statistical analysis of P-values and F-values. If the P-value of the significant coefficient is less than 0.05 or the F-regression is greater than $F_{0.05}$. it indicates that the model developed is highly significant and the confidence interval between the optimized dependent and independent variables is 95%. If the P-value is less than 0.01 or the F-regression is greater than $F_{0.01}$, it indicates that the established model is extremely significant, and the confidence interval between the variables after optimization is 99% (Aziz et al., 2014). Therefore, a second-order response surface model of yield and reaction process parameters was established, and the statistical analysis of the second-order response surface model is shown in Table 3.

As can be seen from Table 3, The F-regression = 90.01 > $F_{0.01}(9,4) = 14.66$, $P < 0.0001$. This indicated that the established second-order multiple regression model was extremely significant. The F misfit = 5.24 < $F_{0.05}(9,3) = 8.81$, the misfit term $P = 0.0717 > 0.05$. This indicated that the established second-order multiple regression model misfit was significant, and the regression equation was fitted to a high degree. In addition, the P-values of primary terms X_1, X_2, X_3 and secondary terms X_1^2, X_2^2, X_3^2 were less than 0.05 indicating that all were significant. Also, from the F-values of primary terms X_1, X_2 and X_3, it is clear that the order of significance of the reaction process parameters on the yield was temperature > molar ratio > catalyst addition. It can be seen from the results of the model that the coefficient of determination R^2 and the adjusted coefficient of determination R^2_{adj} were 0.9914 and 0.9804, respectively. The results indicated that the model had a good fit and can be used to optimize and predict the process parameters for the synthesis of UHT-EM.

The satisfaction of the second-order response surface model can be determined by the normal distribution of the residuals. Fig. 6 shows the relationship between actual and predicted yields, and it can be seen from Fig. 6 that all points were distributed near the fitted line. The results showed that the model was reasonable and the predicted data have credibility.

3.6. Interaction between variable factors

Through the second-order response surface model, it can be found that the molar ratio, temperature and catalyst addition had a significant effect on the yield of the reaction (Guan et al., 2017).

Table 3
Statistical analysis of second order response surface model.

Source	Sum of squares	Free degree	Mean square	F-value	P-value
Model	257.04	9	28.56	90.01	<0.0001
X_1	29.57	1	29.57	93.19	<0.0001
X_2	68.21	1	68.21	214.98	<0.0001
X_3	14.63	1	14.63	46.12	0.0003
X_1X_2	2.92	1	2.92	9.22	0.0190
X_1X_3	0.2809	1	0.2809	0.8853	0.3781
X_2X_3	1.21	1	1.21	3.81	0.0918
X_1^2	52.68	1	52.68	166.02	<0.0001
X_2^2	53.12	1	53.12	167.43	<0.0001
X_3^2	20.42	1	20.42	64.35	<0.0001
Residual	2.22	7	0.3173		
Lack of fit	1.77	3	0.5902	5.24	0.0717
Pure error	0.4505	4	0.1126		
Total error	259.26	16			
R^2	0.9914				
R^2_{Adj}	0.9804				

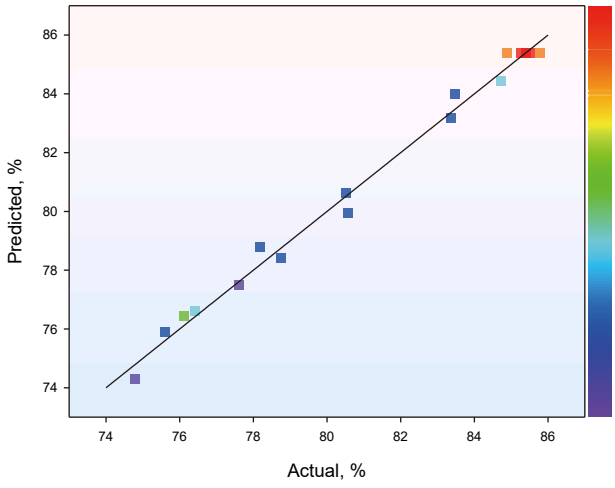

Fig. 6. Relationship between actual and predicted values.

Therefore, in order to reflect more accurately the effects of process parameters on the yield, the interactions between the factors were investigated by response surface methodology. The experimental results are shown in Fig. 7.

Fig. 7(a) and (b) show the 3D surface and contour plots of the effect of molar ratio and temperature on the yield for a certain catalyst addition. It can be seen from Fig. 7(a) that the yield increased gradually with the increase of molar ratio and temperature. The results showed that the maximum reaction yield was achieved when the reaction temperature was between 48 and 54 °C and the molar ratio was between 1.6 and 1.9. It can be seen from Fig. 7(b) that the contour lines towards temperature were denser than those towards molar ratio, and the shape of the contour lines was elliptical. The results showed that the effect of temperature on the yield was larger than that of molar ratio, and the interaction of the two factors had a more significant effect on the yield. This is mainly attributed to the fact that at a certain catalyst addition, the temperature provided a higher activation energy, which intensified the effective collision between molecules and achieved the generation of the target product to satisfy the increase in yield.

Fig. 7(c) and (d) show the 3D surface and contour plots of the effect of molar ratio and catalyst addition on the yield at a certain reaction temperature. It can be seen from Fig. 7(c) that the yield increased gradually with the increase of molar ratio and catalyst addition. The results showed that the maximum reaction yield was achieved when the catalyst addition was between 8% and 14% and the molar ratio was between 1.6 and 1.9. It can be seen from Fig. 7(d) that the contour lines towards the molar ratio direction were denser than those towards the catalyst addition direction, and the contour lines were circular in shape. The results indicated that the effect of molar ratio on yield was greater than that of catalyst dosage, and the effects of molar ratio and catalyst dosage on yield were independent of each other.

Fig. 7(e) and (f) show the 3D surface and contour plots of the effect of temperature and catalyst addition on the yield at certain molar ratio. It can be seen from Fig. 7(e) that the reaction yield increased gradually with the increase of temperature and catalyst addition. The results showed that the maximum reaction yield was achieved when the catalyst dosage was between 8% and 14% and the temperature was between 48 and 54 °C. It can be seen from Fig. 7(f) that the density of contour lines towards temperature was higher than that towards catalyst dosage, and the shape of

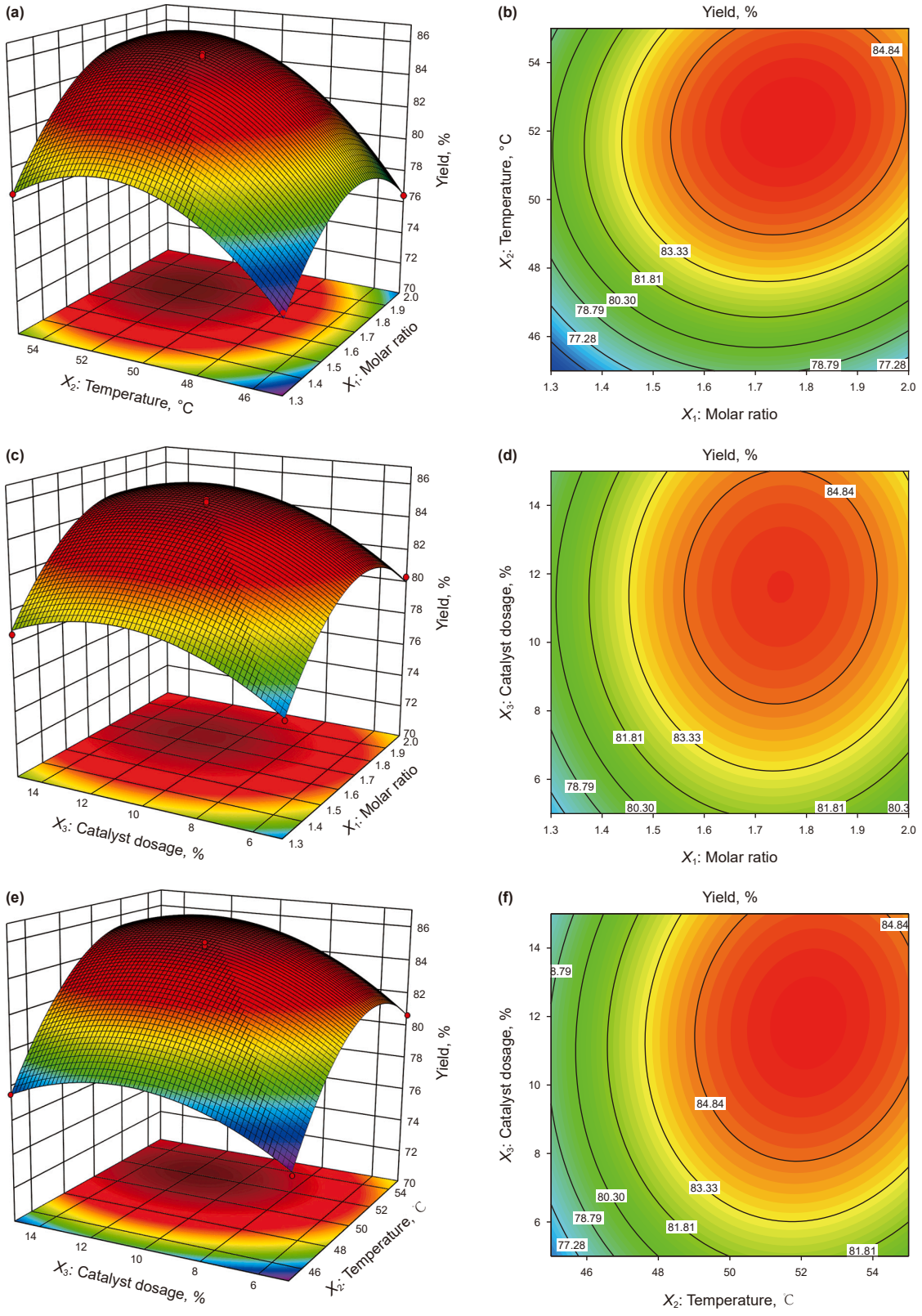

Fig. 7. 3D surface and contour plots of reaction conditions and yield.

contour lines was elliptical. The results showed that the effect of temperature on the yield was greater than that of catalyst dosage, and the mutual effect of temperature and catalyst dosage on the yield was more significant. This is mainly attributed to the fact that temperature could exacerbate effective collisions between molecules and may affect the selectivity of the catalyst.

Fig. 8 shows the optimal synthesis conditions obtained from the Box-Behnken model. The molar ratio was 1.80919, the

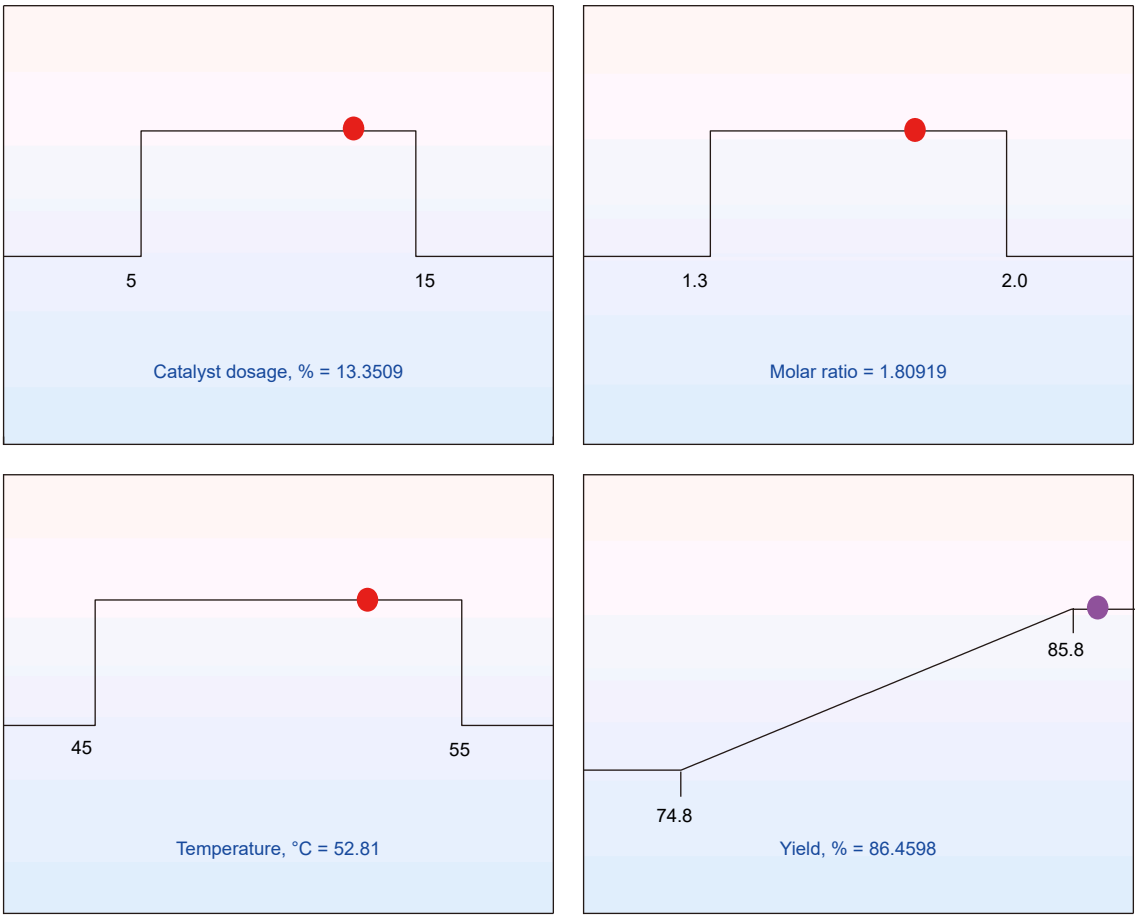

Fig. 8. Optimal factor analysis and yield prediction diagram.

temperature was 52.81 °C, the catalyst dosage was 13.3509%, and the predicted yield was 86.4598%. In order to verify the error between the predicted yield and the actual yield. The molar ratio was 1.8, the temperature was 53 °C, and the catalyst dosage was 13.4% as the reaction conditions. The actual yield was 85.23%, with a relative error of 1.4%. This error was small, indicating that the accuracy of the modeled parameters established by the method was informative.

3.7. Oil water interface tension test

Interfacial tension is a key parameter for evaluating emulsion stability. A lower value indicates higher adsorption efficiency of the emulsifier at the oil-water interface, thereby contributing to the formation of a more stable emulsion. The variation in interfacial tension with different UHT-EM dosages was analyzed, as shown in Fig. 9. It can be observed from Fig. 9 that when the dosage of UHT-EM was 0.5%, the interfacial tension was 3.48 mN·m. As the dosage increased to 1%, the interfacial tension significantly decreased to 1.86 mN·m. With a further increase to 1.5%, the interfacial tension dropped to 1.75 mN·m. When the dosage reached 2% and 2.5%, the interfacial tension stabilizes at 1.73 mN·m. The results indicated that as the dosage of UHT-EM increased, the interfacial tension exhibited an initial rapid decline, followed by a plateau. Specifically, when the dosage was raised from 0.5% to 1%, the interfacial tension decreased by approximately 46.6%. This suggested that the UHT-EM effectively reduced the interfacial energy under the experimental

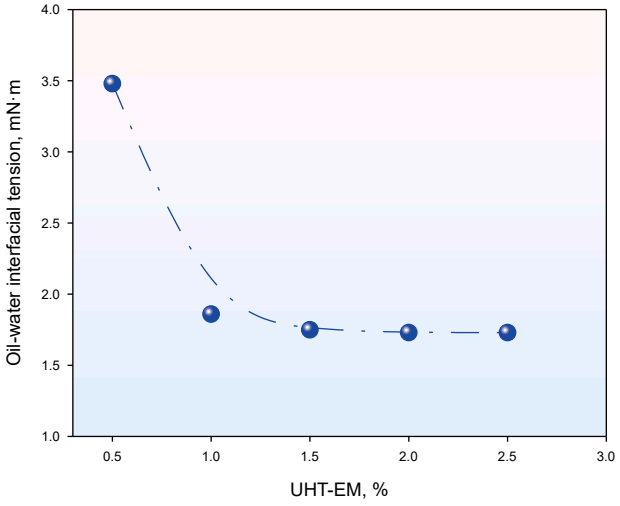

Fig. 9. Effect of UHT-EM on oil-water interfacial tension.

temperature conditions, likely due to the rapid adsorption of UHT-EM molecules at the interface, which consequently lowered the interfacial tension. When the dosage was increased from 1% to 1.5%, the interfacial tension decreased by a smaller margin of approximately 5.9%. This suggested that interfacial adsorption was gradually approaching saturation. Furthermore, when the dosage exceeded 1.5%, the interfacial tension stabilized at 1.73 mN·m with

no significant further changes. This plateau in interfacial tension beyond a dosage of 1.5% likely indicated that UHT-EM had reached its critical micelle concentration (CMC), corresponding to a state of interfacial saturation. At this point, the oil-water interface was fully occupied, and any additional emulsifier molecules could no longer contribute to further tension reduction. Instead, they primarily aggregated to form micelles within the bulk oil phase. This behavior is consistent with the typical surfactant adsorption–micellization transition, beyond which interfacial properties stabilize while excess emulsifier contributes to micellar structures rather than interfacial activity (Mahmoud et al., 2021).

3.8. The temperature resistance of UHT-EM

The rheological properties and ES of the emulsion were analyzed after aging at 230 °C for 16 h, confirming the significant impact of UHT-EM dosage on system stability.

As shown in Fig. 10, the rheological parameters of the emulsion exhibited systematic changes as the dosage of ultra-high-temperature emulsifier increases from 0.5% to 2.5%. The AV steadily increased from 13.00 mPa·s to 22.50 mPa·s, while the PV rose from 8.00 mPa·s to 13.00 mPa·s before stabilizing. It is worth noting that the changes in YP (YP, calculated from the difference between AV and PV) reveal the evolution of the internal structure of the emulsion. At a dosage of 0.5%, YP was 5.00 Pa, and then maintained at 4.50 Pa at 1.0% and 1.5%, indicating the formation of a moderate three-dimensional network structure. However, when the dosage increased to 2.0% and 2.5%, YP significantly increased to 7.00 Pa and 9.50 Pa, respectively. This excessively high YP indicated that the system might have formed an overly rigid structure, which was likely to compromise the stability of the emulsion. Meanwhile, the ES exhibited a trend of first increasing and then decreasing with increasing dosage. It reached a maximum value of 1431 V at 1.0% and remained at a relatively high level (1410 V) at 1.5%. However, when the dosage continued to increase to 2.0% and 2.5%, the ES significantly decreased to 1240 V and 1045 V, respectively. This indicated that excessive surfactant concentration could actually compromise the electrical stability of the emulsion. The decrease in ES at higher UHT-EM dosage (>1.0 %) could be attributed to several interrelated factors. First, once the critical micelle concentration (CMC) was exceeded, a significant fraction of surfactant molecules formed micelles in the bulk oil phase rather than adsorbing at the oil-water interface. This reduced the effective interfacial packing density and weakened the mechanical strength of the interfacial film. Second, excessive surfactant could lead to over-saturation and disorder at the interface, causing electrostatic repulsion between similarly charged headgroups (sulfonate anions) to dominate, which disrupted the compact arrangement of the interfacial layer. Third, high surfactant loading increased the ionic strength near the interface due to the dissociation of calcium sulfonate, which could compress the electrical double layer and reduce the electrostatic barrier against droplet coalescence (Long et al., 2025). These effects collectively degraded the emulsion's ability to withstand an external electric field, thereby lowering the measured ES value. Based on the combined rheological properties and electrical stability metrics, when the emulsifier dosage ranged from 1.0% to 1.5%, the emulsion exhibited both suitable rheological characteristics (AV approximately 15.50–17.50 mPa·s, PV approximately 11.00–13.00 mPa·s, YP approximately 4.50 Pa) and optimal electrical stability (ES > 1400 V). Particularly at 1.0%, the emulsion exhibited the best overall performance. Therefore, the optimal dosage of UHT-EM was determined to be approximately 1.0%. This ratio provided the emulsion with the best overall stability under ultra-high-temperature conditions.

The rheological properties and ES of UHT-EM emulsion, BCEM emulsion, and Span80 emulsion treated at different aging temperatures (230 °C to 260 °C) for 16 h were analyzed to clearly evaluate the temperature resistance of the emulsifier system.

As shown in Fig. 11, the UHT-EM emulsion exhibited good rheological properties and electrical stability after high-temperature aging, demonstrating superior high-temperature emulsification performance compared to BCEM and Span 80. Moreover, the rheological properties of the UHT-EM emulsion exhibited a certain degree of tolerance as the aging temperature increases from 230 °C to 250 °C. The AV gradually increased from 15.50 mPa·s to 20.00 mPa·s. This may be due to the cross-linking of lotion components at ultra-high temperature, indicating that the structural integrity of the emulsion can be maintained within a certain range. Meanwhile, the ratio of YP/PV reached relatively high levels of 0.41 and 0.43 at 230 °C and 250 °C, respectively, indicating that the emulsion maintained good internal dispersion structure and suspension stability within this temperature range. However, when the aging temperature was further increased to 260 °C, the AV of the emulsion decreased from 20.00 mPa·s to 11.25 mPa·s, a reduction of 43.75%. Meanwhile, the YP/PV

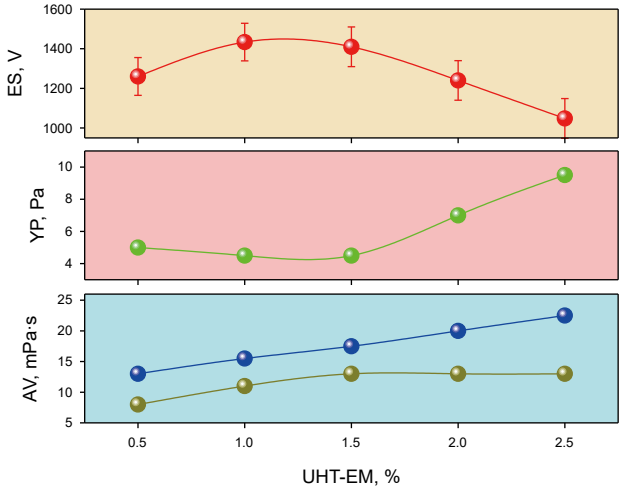

Fig. 10. Dosage optimization of UHT-EM.

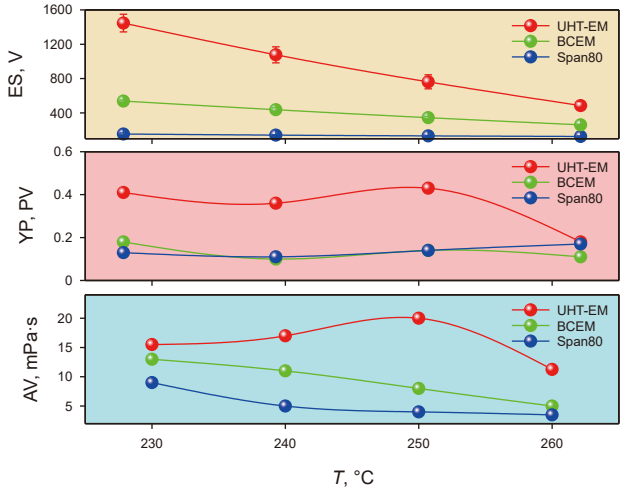

Fig. 11. Temperature resistance of UHT-EM.

decreased from 0.43 to 0.18, a reduction of 58.14%. This indicated that the emulsifier system had approached its tolerance limit, with its internal structure damaged under extreme thermal stress, causing the emulsion to lose its proper rheological properties. More notably, ES showed a continuous downward trend with increasing temperature, significantly decreasing from 1431 V at 230 °C to 430 V at 260 °C. This pattern indicated that ultra-high temperature exacerbated the instability process at the oil-water interface, significantly reducing the stability of the emulsion.

3.9. Wetting performance

Based on the test results of the contact angle of the emulsion at different aging temperatures, the adsorption behavior of the UHT-EM at the oil-water interface and its mechanism of influencing emulsion stability can be thoroughly revealed, as shown in Fig. 12.

As shown in Fig. 12, the contact angle of the emulsion increased continuously from 47.59° to 77.78° as the aging temperature rose from 230 °C to 250 °C. This was primarily attributed to the enhanced competitive adsorption effect of emulsifier molecules at the oil-water interface under high-temperature conditions, leading to a more tightly oriented arrangement. This significantly enhanced the mechanical strength and compactness of the interfacial film, enabling the emulsion to maintain excellent interfacial stability even at ultra-high temperature. However, when the aging temperature further increased to the critical condition of 260 °C, the contact angle sharply decreased to 33.2°, reflecting a fundamental reversal of the wettability of the system. This mutation indicated that after exceeding the temperature resistance limit of the emulsifier, the intense molecular thermal motion caused by high temperature dominates the interfacial process, promoting the desorption of emulsifier molecules (Pu et al., 2022). Moreover, the original compact interface structure was destroyed, and the strength of the interface facial mask was significantly reduced. The direct consequence was the failure of the interfacial barrier function of the emulsion, resulting in coalescence and demulsification of the oil-water phase, manifested macroscopically as a sudden drop in contact angle and loss of system stability. The wettability change pattern was highly consistent with the conclusion of rheological property degradation and decreased electrical stability in the previous section, jointly verifying that the UHT-EM had reliable interfacial stability performance below 250 °C, but failed at 260 °C due to the instability mechanism dominated by interfacial desorption. Therefore, based on the analysis of wetting behavior, it can be concluded that the reasonable upper limit of temperature resistance for this emulsifier was 250 °C, providing a theoretical basis for its safe application in ultra-high temperature industrial environments.

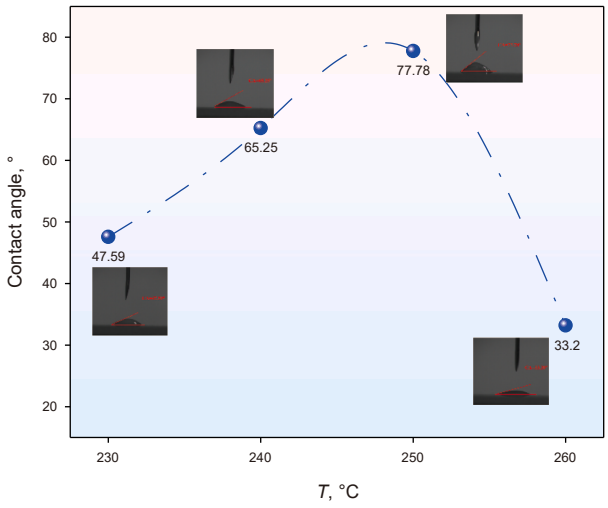

Fig. 12. Contact angle of emulsion.

3.10. Particle size distribution of emulsions

This study delved into the interfacial stabilization mechanism of UHT-EM at the microscopic level and further analyzed the particle size distribution characteristics of emulsions under different aging temperatures.

As shown in Fig. 13, within the temperature range of 230–250 °C, the particle size distribution curve of the emulsion exhibited a single, narrow peak. The primary distribution range was concentrated between 1000 and 2000 nm, with a steeply rising cumulative distribution curve. This indicated uniform droplet size distribution without significant coalescence, maintaining stable emulsion structure. This was primarily attributed to the UHT-EM forming a highly ordered, mechanically robust adsorption layer at the oil-water interface within the 230–250 °C range. Its dodecyl chains inserted into the oil phase via hydrophobic interactions, providing an effective spatial barrier. Meanwhile, the calcium bisulfate groups formed a stable network structure at the interface through ion-pair interactions and π–π stacking between benzene rings (Zhang et al., 2011). This structure effectively resisted high-temperature-induced interface disturbances, thereby inhibiting droplet coalescence and Ostwald ripening.

However, when the temperature rises to 260 °C, the particle size distribution shifted markedly to the right, with a significant increase in peak width. Simultaneously, the cumulative distribution curve flattened. This indicated an increase in the average droplet size and a broadening of the distribution range, suggesting partial droplet coalescence and structural destabilization within the system. This was mainly attributed to the fact that when the temperature reached 260 °C, the thermal kinetic energy had approached or exceeded the tolerance limit of the intermolecular interaction of the UHT-EM. On the one hand, ultra-high temperature may cause the weakening of electrostatic interaction between calcium sulfonate polar head groups, or even thermal dissociation of some ion pairs, resulting in a decrease in the order of molecular arrangement in the interface facial mask (Zenaida et al., 2021). On the other hand, the intense thermal movement of the alkyl chain reduced its anchoring ability in the oil phase, which significantly reduced the compactness and self-healing ability of the interface facial mask (Zhao and Wang, 2017). In addition, the increase in water vapor pressure and the intensification of molecular Brownian motion at high temperatures also led to an increase in droplet collision frequency and energy, further exacerbating the coalescence process, ultimately resulting in an increase in particle size and a wider distribution of the emulsion at the macroscopic level.

3.11. Mechanism analysis

The mechanism of action of UHT-EM is shown in Fig. 14. Under ultra-high temperature conditions, UHT-EM facilitated structural stabilization of the emulsion by forming an ordered and dense adsorption layer at the oil-water interface (Kanae et al., 2012). The didodecyl chains of the emulsifier penetrated into the oil phase through hydrophobic interactions, establishing an effective spatial barrier that suppressed droplet coalescence (Liu et al., 2023). Simultaneously, the calcium disulfonate polar heads constructed a stable interfacial network via ion-pair interactions and π–π stacking between benzene rings, which considerably enhanced the

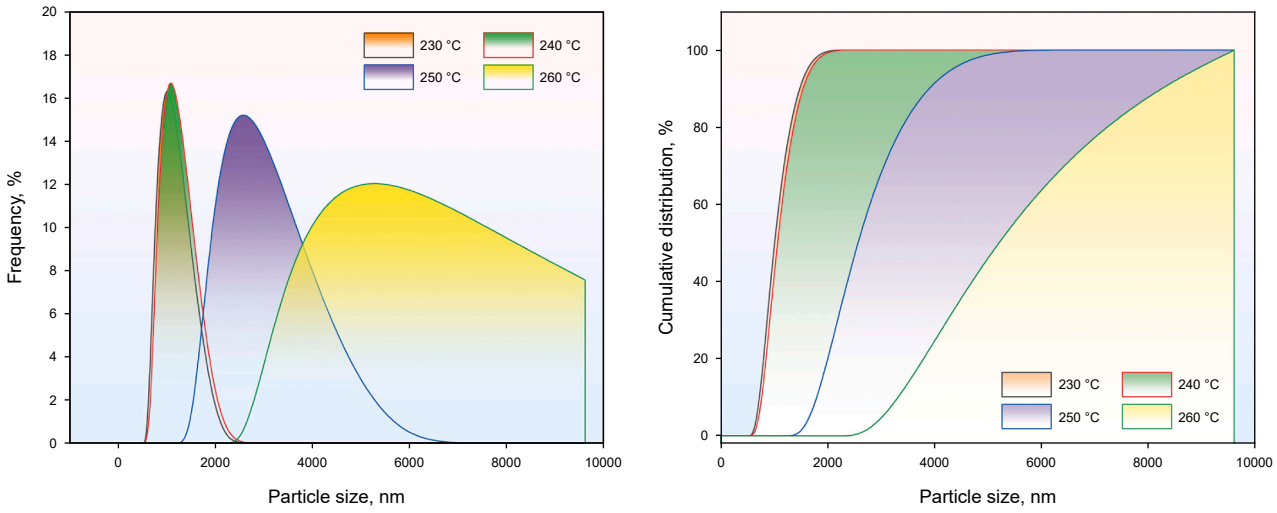

Fig. 13. Particle size distribution of emulsion.

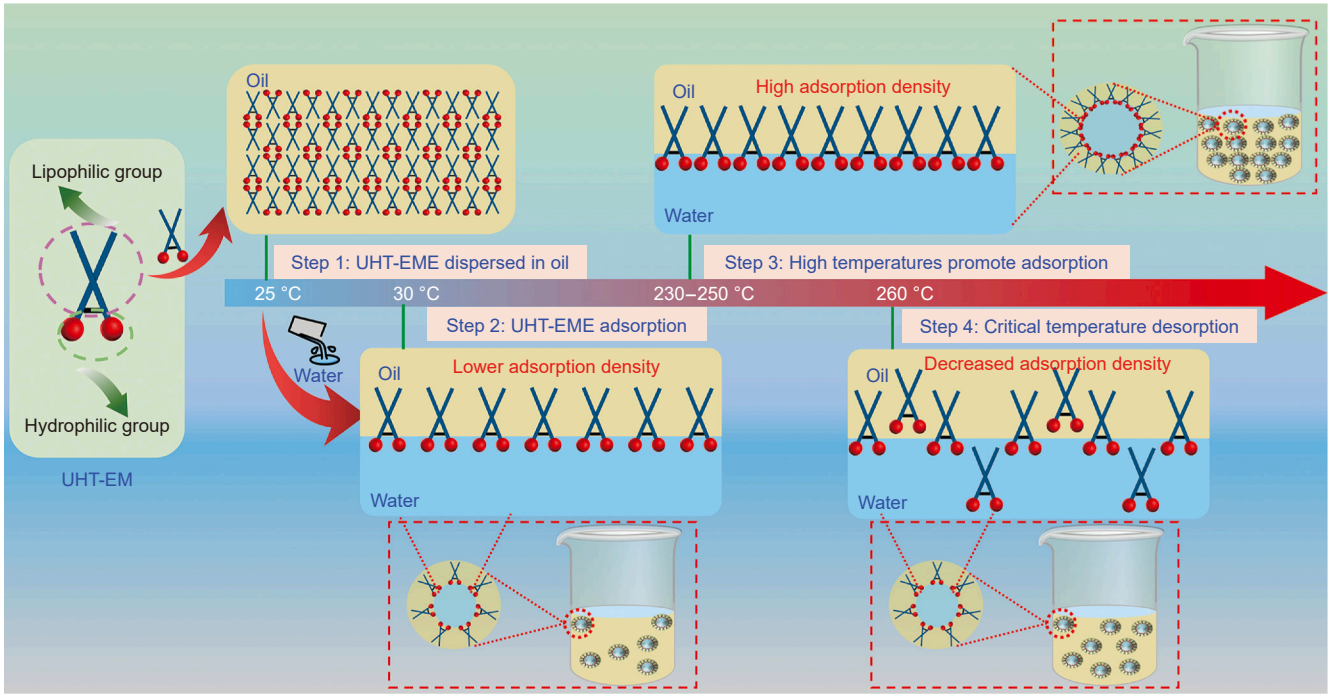

Fig. 14. Schematic diagram of the mechanism of action of UHT-EM.

mechanical strength and compactness of the interfacial film (Qin et al., 2025). Within the temperature range of 230–250 °C, this structural configuration effectively resisted disturbances induced by high temperatures, thereby maintaining uniform droplet size distribution and high electrical stability. However, when the temperature was elevated to 260 °C, intensified molecular thermal motion induced thermal dissociation of ion pairs and weakened the anchoring capacity of the alkyl chains in the oil phase. As a result, the structural order and self-healing capability of the interfacial film were markedly compromised, leading to droplet coalescence, broader particle size distribution, and a sharp decline in electrical stability (Kong et al., 2023; Lv et al., 2025). These findings indicate that the upper temperature limit for UHT-EM under these conditions was 250 °C. Collectively, the study elucidates the emulsification and failure behavior of UHT-EM under ultra-high temperature conditions from three perspectives: interfacial adsorption behavior, structural integrity, and microscopic particle size evolution.

4. Conclusion

This study successfully synthesized a novel ultra-high-temperature emulsifier, UHT-EM, via a three-step synthetic route and systematically investigated its synthesis process, molecular structure, emulsification performance, and thermal resistance mechanism. First, the target product was successfully synthesized through acylation, Friedel–Crafts alkylation, and sulfonation–neutralization reactions. FT-IR analysis confirmed the presence of characteristic structural features, including a benzene ring skeleton, long alkyl chains, and sulfonate groups, while TGA

demonstrated the exceptional thermal stability of the UHT-EM. Second, response surface methodology was employed to optimize key process parameters, establishing a highly significant quadratic regression model. The optimal synthesis conditions were determined as a molar ratio of 1.8, reaction temperature of 53 °C, and catalyst dosage of 13.4%, under which an actual yield of 85.23% was achieved, validating the reliability and feasibility of the optimized process.

Performance evaluation revealed that UHT-EM effectively adsorbed at the oil–water interface and significantly reduced interfacial tension, with a critical micelle concentration of approximately 1.5%. At the recommended dosage of 1.0%, the emulsion exhibited optimal rheological properties and the highest electrical stability (1431 V) after thermal aging at 230 °C. Moreover, comprehensive analysis combining rheology, electrical stability, wettability, and particle size distribution confirmed that the UHT-EM-stabilized emulsion maintained excellent stability up to 250 °C, with an intact interfacial film and uniform droplet distribution. However, when the temperature reached a critical point of 260 °C, intense thermal motion induced molecular desorption and disruption of the interfacial structure, leading to droplet coalescence and eventual emulsion breakdown, thereby establishing an effective operational temperature limit of 250 °C.

In summary, this study successfully developed a high-performance ultra-high-temperature emulsifier and systematically elucidated its stabilization and failure mechanisms using a multi-scale analytical approach, providing important theoretical guidance and practical foundations for the design of ultra-high-temperature drilling fluids. Future work should focus on two key directions to bridge fundamental understanding with engineering application: employing molecular dynamics simulations to clarify its high-temperature interfacial behavior at the atomic scale, and evaluating its integrated performance in fully formulated drilling fluids under realistic downhole conditions featuring combined high temperature, pressure, and salinity.

CRediT authorship contribution statement

Quan-De Wang: Writing – original draft, Methodology, Investigation, Formal analysis, Data curation. **Guan-Cheng Jiang:** Writing – review & editing, Supervision, Funding acquisition. **Teng-Fei Dong:** Writing – review & editing, Supervision, Funding acquisition. **Sheng-Ming Huang:** Writing – review & editing, Validation, Conceptualization. **Yin-Bo He:** Validation, Conceptualization. **Li-Li Yang:** Validation, Conceptualization. **Qi Feng:** Validation, Conceptualization. **Hua-Yan Mu:** Resources, Investigation.

Data availability statement

The data is available upon request.

Declaration of competing interest

The authors declare that they have no known competing financial interests or personal relationships that could have appeared to influence the work reported in this paper.

Acknowledgements

This work was financially supported by the National Natural Science Foundation of China (Grant No. U23B2082) and the Science Foundation of China University of Petroleum, Beijing (Grant No. 2462023SZBH018).

References

Abdullahi, A.N., Muhammad, A.K., Zhang, Y.X., et al., 2025. Modified natural polymers as additives in high-temperature drilling fluids: a review. Int. J. Biol. Macromol. 287, 138556. https://doi.org/10.1016/j.ijbiomac.2024.138556.

Aftab, H.A., Syahrir, R., 2025. Effect of multifunctional boron nitride nanoparticles on the performance of oil-based drilling fluids in high-temperature unconventional formation drilling. Geoenergy Sci. Eng. 247, 213722. https://doi.org/10.1016/j.geoen.2025.213722.

Aziz, N.A.M., Yunus, R., Rashid, U., et al., 2014. Application of response surface methodology (RSM) for optimizing the palm-based pentaerythritol ester synthesis. Ind. Crops Prod. 62, 305–312. https://doi.org/10.1016/j.indcrop.2014.08.040.

Bai, Y., He, J.N., Gu, D., et al., 2025. A silane-grafted silica-oil-absorbing resin (SiO_2-MSS) composite for enhanced lost circulation control in oil-based drilling fluids. J. Mol. Liq. 439, 128867. https://doi.org/10.1016/j.molliq.2025.128867.

Bhola, K.P., Vikas, M., 2020. Development of environment-friendly oil-in-water emulsion-based drilling fluid for shale gas formation using sunflower oil. J. Pet. Sci. Eng. 191, 107129. https://doi.org/10.1016/j.petrol.2020.107129.

Chen, Y.R., Song, Q., Tan, Y.B., 2022. Synthesis, aggregation behavior of alternating copolymer emulsifier in oil solution and its application in oil-based drilling fluids. J. Mol. Liq. 348, 118011. https://doi.org/10.1016/j.molliq.2021.118011.

Du, K., 2020. Development and evaluation of a new high efficiency emulsifier for oil-based drilling fluids. Drill. Fluid Complet. Fluid 37 (5), 555–560 (in Chinese).

Feng, Q., Wang, Q.D., Wang, N.X., et al., 2025. A superhydrophobic gel fracturing fluid with enhanced structural stability and low reservoir damage. Gels 11 (10), 772. https://doi.org/10.3390/gels11100772.

Guan, S., Deng, F., Huang, S.Q., et al., 2017. Optimization of magnetic field-assisted ultrasonication for the disintegration of waste activated sludge using Box–Behnken design with response surface methodology. Ultrason. Sonochem. 38, 9–18. https://doi.org/10.1016/j.ultsonch.2017.02.024.

Huang, J., Huo, Y.J., Li, J.L., et al., 2026. Interface properties and emulsifying properties of cardanol-based zwitterionic surfactants with different alkyl chain length in headgroup: experimental and calculation. J. Mol. Struct. 1349, 143781. https://doi.org/10.1016/j.molstruc.2025.143781.

Jiang, G.C., He, Y.B., Huang, X.B., et al., 2016. A high-density organoclay-free oil base drilling fluid based on supramolecular chemistry. Petrol. Explor. Dev. 43 (1), 143–148. https://doi.org/10.1016/S1876-3804(16)30017-9.

Kanae, N., Tomokazu, Y., Koji, T., et al., 2012. Zwitterionic heterogemini surfactants containing ammonium and carboxylate headgroups 2: aggregation behavior studied by SANS, DLS, and cryo-TEM. J. Colloid Interface Sci. 370 (1), 80–85. https://doi.org/10.1016/j.jcis.2011.12.027.

Kong, L.Y., Yang, M.Z., Wang, H.M., et al., 2023. Study on the effect of sulfonic acid root position on the stability of SDBS emulsified asphalt. Constr. Build. Mater. 396, 132303. https://doi.org/10.1016/j.conbuildmat.2023.132303.

Lei, M., Sun, J.S., Zhu, H.Y., et al., 2024. Synthesis and characterization of natural rosin-modified silica nanocomposite and its green multifunctional applications for drilling fluid. Colloids Surf., A Physicochem. Eng. Asp. 702, 134994. https://doi.org/10.1016/j.colsurfa.2024.134994.

Lei, M., Zhu, H.Y., Cai, Z.X., et al., 2025. Molecular dynamics study on the temperature response of a chitosan-based graft polymer with different grafting densities of oligo (ethylene glycol) methacrylate side chains. Macromolecules 58 (17), 8990–9009. https://doi.org/10.1021/acs.macromol.5c00188.

Li, Y.F., Wang, Y.L., Wang, Q., 2018. Optimization the synthesis parameters of gas-wetting alteration agent and evaluation its performance. Colloids Surf., A Physicochem. Eng. Asp. 558, 438–445. https://doi.org/10.1016/j.colsurfa.2018.08.079.

Li, C., Di, W.W., Geng, T., et al., 2023. A pickering emulsion oil based drilling fluid. Drill. Fluid Complet. Fluid 40 (1), 28–34 (in Chinese).

Liu, L., Pu, X.L., Zhou, Y., et al., 2020. Smart Pickering water-in-oil emulsion by manipulating interactions between nanoparticles and surfactant as potential oil-based drilling fluid. Colloids Surf., A Physicochem. Eng. Asp. 586, 124246. https://doi.org/10.1016/j.colsurfa.2019.124246.

Liu, X.J., Liu, G., Wang, S.N., et al., 2022. Preparation and performance evaluation of emulsifier with high temperature resistance for oil-based drilling fluid. Oilfield Chem. 39 (4), 571–576. https://doi.org/10.19346/j.cnki.1000-4092.2022.04.001 (in Chinese).

Liu, J.B., Liu, S., Zhong, L.G., et al., 2023. Ultra-low interfacial tension Anionic/Cationic surfactants system with excellent emulsification ability for enhanced oil recovery. J. Mol. Liq. 382, 121989. https://doi.org/10.1016/j.molliq.2023.121989.

Liu, J.B., Liu, S., Gao, J., et al., 2026. Exploring the mechanisms of instability and characteristics of interfacial adsorption in oil-in-water emulsions. Chem. Eng. Sci. 319, 122284. https://doi.org/10.1016/j.ces.2025.122284.

Long, Y., Muhsen, S., Hamid, A., et al., 2025. Optimizing the storage stability of emulsified asphalt using electrokinetic potential with emulsifiers of varying ionic characteristics. J. Environ. Chem. Eng. 13 (6), 119427. https://doi.org/10.1016/j.jece.2025.119427.

Lv, M., Chu, J.Z., Cui, C.Y., et al., 2025. Magnetic-thermal dual-responsive nanoparticle emulsification and interfacial properties study and their microscopic processes in oil-water systems. Mater. Today Commun. 49, 114348. https://doi.org/10.1016/j.mtcomm.2025.114348.

Ma, S.Z., Zhang, Y.Y., Nan, Y., et al., 2025. Synthesis and performance evaluation of main emulsifier OBE-2 for oil-based drilling fluid. Chem. Eng. 39 (2), 53–58. https://doi.org/10.16247/j.cnki.23-1171/tq.20250253 (in Chinese).
Mahmoud, M., Fayad, D.E., Mohamed, E.A., et al., 2021. Optimization of invert emulsion oil-based drilling fluids performance through heterocyclic imidazoline-based emulsifiers. Colloids Surf., A Physicochem. Eng. Asp. 613, 126092. https://doi.org/10.1016/j.colsurfa.2020.126092.
Marinescu, P., Young, S., Iskander, G.R., 2014. New generation ultra-high temperature synthetic-based drilling fluid; Development and best practices for extreme conditions and ECD management. SPE 5, 3894–3908. https://doi.org/10.2118/172056-MS.
Meng, X., Huang, X.B., Sun, J.S., et al., 2025. Ultra-high temperature resistant polystyrene/acrylic resin microspheres for enhanced wellbore stability of oil-based drilling fluids. Colloids Surf., A Physicochem. Eng. Asp. 725, 137637. https://doi.org/10.1016/j.colsurfa.2025.137637.
Mona, K., Javad, S., Morteza, T., et al., 2023. Molecular design and applications of a nanostructure green tripodal surface active ionic liquid in enhanced oil recovery: interfacial tension reduction, wettability alteration, and emulsification. Pet. Sci. 20 (6), 3530–3539. https://doi.org/10.1016/j.petsci.2023.07.010.
Ni, X.X., Shi, H., Zhang, J.Q., et al., 2023. Modified Laponite synthesized with special wettability as a multifunctional additive in oil-based drilling fluids. J. Pet. Sci. Eng. 220, 111211. https://doi.org/10.1016/j.petrol.2022.111211.
Nilanjan, P., Neha, S., Laxmi, K.V.D., et al., 2018. Interfacial behaviour, wettability alteration and emulsification characteristics of a novel surfactant: implications for enhanced oil recovery. Chem. Eng. Sci. 187, 200–212. https://doi.org/10.1016/j.ces.2018.04.062.
Pu, L., Xu, P., Xu, M.B., et al., 2022. Enhanced stability of low oil-to-water ratio water-in-oil emulsions (oil-based drilling fluids): synergistic effect of nano-SiO_2 and emulsifiers. J. Pet. Sci. Eng. 219, 111053. https://doi.org/10.1016/j.petrol.2022.111053.
Qin, W.Q., Liu, Y.F., Gang, H.Z., et al., 2025. Structural diversity of surfactin lipopeptides and their molecular behaviors in solutions and at interfaces. Adv. Colloid Interface Sci. 343, 103581. https://doi.org/10.1016/j.cis.2025.103581.
Sun, J.S., Wang, J.H., 2025. Drilling fluid technology for deep subsurface Tako-1 well. Drill. Fluid Complet. Fluid 42 (2), 155–166 (in Chinese).
Sun, J.S., Huang, X.B., Jiang, G.C., et al., 2018. Development of key additives for organoclay-free oil-based drilling mud and system performance evaluation. Petrol. Explor. Dev. 45 (4), 764–769. https://doi.org/10.1016/S1876-3804(18)30079-X.
Sun, J.S., Yang, J.B., Bai, Y.R., et al., 2024. Research progress and development of deep and ultra-deep drilling fluid technology. Petrol. Explor. Dev. 51 (4), 1022–1034. https://doi.org/10.1016/S1876-3804(24)60522-7.
Tu, R., 2016. Preparation and Performance Study of an Emulsifier for Star Shaped Oil-based Drilling Fluid. Southwest Petroleum University, Chengdu, China (in Chinese).
Wang, H.G., Huang, H.C., Bi, W.X., et al., 2022. Deep and ultra-deep oil and gas well drilling technologies: progress and prospect. Nat. Gas. Ind. B. 9 (2), 141–157. https://doi.org/10.1016/j.ngib.2021.08.019.
Wang, Y.P., Li, M.X., Hou, J., et al., 2022. Design, synthesis and properties evaluation of emulsified viscosity reducers with temperature tolerance and salt resistance for heavy oil. J. Mol. Liq. 356, 118977. https://doi.org/10.1016/j.molliq.2022.118977.
Wang, G.S., Jiang, G.C., Fu, Y., et al., 2022. pH-responsive water-in-oil emulsions with reversible phase inversion behavior stabilized by a novel dynamic covalent surfactant. J. Mol. Liq. 364, 120004. https://doi.org/10.1016/j.molliq.2022.120004.
Wang, Q.D., Michal, S., Gu, X.F., et al., 2022. Lubricity and rheological properties of highly dispersed graphite in clay-water-based drilling fluids. Materials 15 (3), 1083. https://doi.org/10.3390/ma15031083.
Wang, J.H., Sun, Y.Q., Zhou, J.J., 2023. Preparation of a new polymeric surfactant and its thickening of the linear alkylbenzene sulfonate system. J. Mol. Liq. 379, 121694. https://doi.org/10.1016/j.molliq.2023.121694.
Wang, Q.D., Chang, Z.L., Li, Y.F., et al., 2025. Study on a novel cationic polyether amine with multi-dimensional synergistic inhibition of wellbore instability. J. Mol. Liq. 428, 127518. https://doi.org/10.1016/j.molliq.2025.127518.
Xie, W.Q., Hu, J.W., Yang, J., et al., 2026. Intelligent snowman-shaped pH-responsive Janus emulsifier: preparation and emulsification properties. Colloids Surf., A Physicochem. Eng. Asp. 729, 138841. https://doi.org/10.1016/j.colsurfa.2025.138841.
Yang, L.L., Wu, Y.P., Liu, Z.Y., et al., 2025. Preparation, characterization and application of modified barite grafted with lipophilic polymers for oil-based drilling fluids. Geoenergy Sci. Eng. 251, 213882. https://doi.org/10.1016/j.geoen.2025.213882.
Zenaida, B.A., Soltero-Martínez, J.F.A., Castillo, R., 2021. Aqueous foams and emulsions stabilized by mixtures of silica nanoparticles and surfactants: a state-of-the-art review. Chem. Eng. J. Adv. 7, 100116. https://doi.org/10.1016/j.ceja.2021.100116.
Zhang, Q., Tian, M.Z., Han, Y.C., et al., 2011. Synthesis, aggregation behavior and interfacial activity of branched alkylbenzenesulfonate gemini surfactants. J. Colloid Interface Sci. 362 (2), 406–414. https://doi.org/10.1016/j.jcis.2011.05.087.
Zhang, R., Huo, J.H., Peng, Z.G., et al., 2017. Emulsification properties of comb-shaped trimeric nonionic surfactant for high temperature drilling fluids based on water in oil. Colloids Surf., A Physicochem. Eng. Asp. 520, 855–863. https://doi.org/10.1016/j.colsurfa.2017.01.017.
Zhang, T.F., Sun, J.S., Liu, J.P., et al., 2025. High-temperature and high-salinity resistance hydrophobic association zwitterionic filtrate loss reducer for water-based drilling fluids. Pet. Sci. 22 (7), 2851–2867. https://doi.org/10.1016/j.petsci.2025.05.016.
Zhao, W.W., Wang, Y.L., 2017. Coacervation with surfactants: from single-chain surfactants to Gemini surfactants. Adv. Colloid Interface Sci. 239, 199–212. https://doi.org/10.1016/j.cis.2016.04.005.
Zhao, Q.Z., Lan, Q., Zheng, C.S., 2023. Research and development of emulsifiers for oil-based drilling fluids. Shandong Chem. Ind. 52 (7), 88–90. https://doi.org/10.19319/j.cnki.issn.1008-021x.2023.07.043 (in Chinese).
Zhu, S.X., Kong, L.Y., Peng, Y., et al., 2025. Multi-scale simulation and experimental study on the stability mechanisms of emulsifiers at the asphalt-water interface: electrophilic/nucleophilic effect. Colloids Surf., A Physicochem. Eng. Asp. 721, 137185. https://doi.org/10.1016/j.colsurfa.2025.137185.